

Cone-beam CT to Planning CT synthesis using generative adversarial networks

S Kida¹‡, S Kaji^{1,2}‡, K Nawa¹, T Imae¹, T Nakamoto¹, S Ozaki¹, T Ohta¹,
Y Nozawa¹ and K Nakagawa¹

¹ Department of Radiology, University of Tokyo Hospital, 7-3-1, Hongo, Bunkyo-ku, Tokyo, 113-0033, Japan

² Institute of Mathematics for Industry, Kyushu University, 744 Motooka, Nishi-ku, Fukuoka, 819-0395, Japan / JST PRESTO

E-mail: satoshikida1492@gmail.com

Abstract. Cone-beam computed tomography (CBCT) offers advantages over conventional fan-beam CT in that it requires a shorter time and less exposure to obtain images. CBCT has found a wide variety of applications in patient positioning for image-guided radiation therapy, extracting radiomic information for designing patient-specific treatment, and computing fractional dose distributions for adaptive radiation therapy. However, CBCT images suffer from low soft-tissue contrast, noise, and artifacts compared to conventional fan-beam CT images. Therefore, it is essential to improve the image quality of CBCT. In this paper, we propose a synthetic approach to translate CBCT images with deep neural networks. Our method requires only unpaired and unaligned CBCT images and planning fan-beam CT (PlanCT) images for training. Once trained, 3D reconstructed CBCT images can be directly translated to high-quality PlanCT-like images. We demonstrate the effectiveness of our method with images obtained from 20 prostate patients, and we provide a statistical and visual comparison. The image quality of the translated images shows substantial improvement in voxel values, spatial uniformity, and artifact suppression compared to those of the original CBCT. The anatomical structures of the original CBCT images were also well preserved in the translated images. Our method enables more accurate adaptive radiation therapy, and opens up new applications for CBCT that hinge on high-quality images.

1. Introduction

Cone-beam computed tomography (CBCT) uses a wide, cone-beam of X-rays and offers considerable advantages insofar as the volume information of patients can be obtained more quickly and with lower exposure. Compared to conventional fan-beam CT, however, the image quality of CBCT is degraded due to X-ray scattering and truncated projections, hindering the effective use of CBCT in many potential applications. It is therefore important to improve the image quality of CBCT.

The most popular use of CBCT in modern radiation therapy is for patient positioning in image-guided radiation therapy [4, 18, 8, 34]. CBCT imaging systems can be incorporated

‡ The two authors contributed equally to this work.

into a conventional radiotherapy device, since they are inexpensive and compact. Usually, planning fan-beam CT (PlanCT) images with high resolution for treatment planning in radiation therapy are acquired once before the course of treatment. On the other hand, CBCT images are acquired just before each radiation treatment along the fractional irradiations on the treatment couch to provide up-to-date anatomical information regarding the patients. Patient setup for radiation therapy is performed by manual or automatic image registration between CBCT and PlanCT using target registration software. However, the quality of image registration often depends on the experience and intuition of the operator, because the image quality of CBCT is insufficient for identifying the structure of organs within soft tissue.

Recently, possible applications of CBCT for patient-specific treatment have also been explored. The CBCT images acquired during each treatment can include information on the patient's condition and the response to the treatment. Several methods of quantitative radiomic analysis using CBCT have been reported [9, 32]. However, the low image quality of CBCT may prevent the accurate extraction of such radiomic information.

The effective use of CBCT for adaptive radiation therapy (ART) has also been studied. In addition to CBCT, many approaches to the implementation of ART have been investigated that allow adaptive treatment change based on patient anatomy. Although CBCT images provide up-to-date information regarding patients, they have not been used directly to compute dose distributions for re-planning in ART owing to their low image quality [26, 19]. The conventional approach to dose calculation using CBCT is to transform PlanCT images to CBCT images using deformable image registration (DIR) and then calculate the dose distribution using the transformed PlanCT [10, 6, 29]. Another approach to dose calculation using CBCT is to compute the dose distribution directly with the improved CBCT images [31]. Improving the CBCT image quality while preserving the anatomical structures of CBCT should be effective for both approaches.

It is essential to improve the image quality of CBCT image for the overall accuracy of radiotherapy. Several methods have been applied to remove the scatter photons from CBCT 2D projection images, such as hardware suppression using an anti-scatter grid and software estimation using a scatter deconvolution technique [31, 3, 20]. On the other hand, a different approach has been proposed, which uses PlanCT as prior information to improve the quality of CBCT images. This approach is applicable to direct 3D image reconstruction with sparse sampling [17], histogram matching [11], super-resolution [2], and a deep convolutional neural network [25]. Although these do not require access to the raw projection data or a particular scanner manufacturer, they depend on accurate spatial alignment of CBCT and PlanCT volume pairs from the same patients. Misalignments between paired images can lead to errors like edge blurring, deformation, and the disappearance of some anatomical structures in the improved CBCT images. However, it is challenging to achieve sufficiently accurate alignments between CBCT and PlanCT images even for the same patient, because these images are clinically acquired on different days separated by days or weeks.

Deep neural networks (DNNs) have been successfully applied to various image processing tasks [21, 30]. In particular, the generative adversarial network (GAN) has been widely used for image translation such as image style transfers [24]. Conditional GAN is

an approach to learning translation mapping with a conditional setting to capture structural information [23]. The objective of a conditional GAN is adversarial loss combined with a voxel-wise loss of the aligned paired images. Nie et al. have applied the idea of combining voxel-wise loss with adversarial loss to translating brain MRI to CT images. As a result, high-quality, less blurry CT images were synthesized [5]. However, voxel-wise loss also depends on the accuracy of the alignment of paired images, and it is clinically difficult, if not impossible, to acquire aligned paired training images from two different modalities. To learn the translation mappings in the absence of aligned paired images, a cycle-consistency GAN (CycleGAN) [15] has been proposed. In this paper, we adapt CycleGAN to synthesize PlanCT-like images (SynPlanCT) from CBCT images with unpaired and unaligned CBCT and PlanCT training datasets.

Suppose we have two sets of images from two domains, X and Y . It should be emphasized that we do not require any prescribed correspondence between the elements of X and Y . To translate CBCT and PlanCT images, we need only independent images from CBCT and PlanCT, and these may be taken on different days from different patients. We only require that each set is consistent and uniform. CycleGAN learns a mapping $G_{X \rightarrow Y} : X \rightarrow Y$ and $G_{Y \rightarrow X} : Y \rightarrow X$, such that the distributions (or characteristics) of images from the output of $G_{X \rightarrow Y}$ (and, respectively, of $G_{Y \rightarrow X}(Y)$) are indistinguishable from that of Y (and, respectively, X) using an adversarial loss. In addition, a cycle-consistency loss is introduced to force the network to translate the synthesized image back to the original image domain and minimize the difference between the original input image and the reproduced image. This scheme has intrinsic ambiguity with respect to geometric transformation, which may fail to preserve the anatomical structure in transformed medical images. To mitigate this problem, methods such as shape-consistency loss [35] have been introduced to constrain the geometric invariance of synthesized images. However, this requires additional input data (segmentation), which is unavailable in our case insofar as the quality of CBCT images is insufficient to perform reliable segmentation.

Recently, CycleGAN has been used to synthesize CT images from MR images and various network structures and loss functions have been proposed [5, 14]. To our knowledge, however, there has been no research regarding adapting CycleGAN to synthesize PlanCT images from CBCT images. MR images offer higher contrast relative to CT images. Therefore, synthesizing CT from MR images can be performed by reducing the amount of information. On the other hand, compared to CT images, CBCT images have low soft-tissue contrast, noise, and artifacts that spread across on the entire image. In this sense, a non-trivial extension to the network algorithm beyond that of previous works should be constructed in order to synthesize CT from CBCT images.

In this paper, we propose a synthetic approach to producing SynPlanCT images from CBCT images. The proposed method relies exclusively on unpaired and unaligned image datasets. The proposed approach is largely based on CycleGAN, and the network structure and the loss functions were determined through trial and error while observing the image quality of the SynPlanCT images. The image quality of SynPlanCT images was quantitatively evaluated in terms of their voxel values and spatial uniformity. We analyzed the extent to

which they preserved the anatomical structures through a comparison with the original CBCT images. The robustness of our method was confirmed by investigating SynPlanCT images from five network models trained with the same structure and hyper-parameter settings. To the best of our knowledge, this is the first study that attempts to translate CBCT images to PlanCT images with a DNN using only unpaired and unaligned training data.

The remainder of this paper is organized as follows. In §2, we explain how we collected and processed image data to train our neural networks, and we provide details regarding the neural networks based on CycleGAN. We also discuss the evaluation of our method, which is based on comparing the ROI from the images. In §3, we present the output of our method and some statistics related to its evaluation. In §4, we focus on the evaluation, specifically the robustness of our method and its improvement in image quality. In §5, we summarize our findings.

2. Materials and Methods

2.1. Data acquisition and image processing

In this study, we used CBCT and PlanCT image pairs from 20 prostate cancer patients who underwent stereotactic radiotherapy with an Elekta Synergy linear accelerator (Elekta AB, Stockholm, Sweden). The PlanCT images had a matrix size of 512 by 512 on the axial plane with a pixel size of 1.074 mm by 1.074 mm and a slice thickness of 1 mm. We used between 170 and 210 slices per patient. CBCT images were acquired during the course of the treatment using a kV on-board imager (XVI) with a tube voltage 120 kV and an exposure of 350 mAs. These were output to match the resolution and the slice thickness of the PlanCT images automatically using XVI. PlanCT images were acquired only once, about two weeks before the course of treatment. Among the images from the 20 patients, those from 4 patients (referred to hereafter as (i)–(iv)) were kept for evaluation, and those from the remaining 16 patients were used to train the network. We used a total of 2795 CBCT images and 2795 PlanCT images for training, although these numbers did not need to be same.

Preprocessing to create training CBCT and PlanCT images was performed as follows. To avoid any adverse impact from non-anatomical structures on a CBCT-to-PlanCT registration and as a model training procedure, binary masks were created to separate the pelvic region from non-anatomical regions. These masks were generated by applying the Otsu auto-thresholding method on each CBCT and PlanCT image. The voxel values outside the mask region were entirely replaced with a Hounsfield Unit (HU) of -1000. Then, the masked PlanCT volume data for each patient were three-dimensionally pre-aligned to each of the masked CBCT images by rigid registration using open-source software called Elastix [27]. Though CycleGAN does not require aligned paired images of CBCT and PlanCT, 3D pre-alignment was performed such that the bodies of all patients were included in a cropped calculation area around the center with a size of 480×384 for efficient calculation. Cropping was performed randomly around the center for each epoch of training. Finally, the voxel values were clipped to the range of $[-500, 200]$ for efficiency.

2.2. Image synthesis with deep neural network

We regard a (volumetric) CT image in any modality as an array $\mathbb{R}^{h \times w \times d}$, where $h \times w$ is the slice dimension and d is the number of slices. Image synthesis (or conversion) can be considered as a mapping $\mathbb{R}^{h_1 \times w_1 \times d_1} \rightarrow \mathbb{R}^{h_2 \times w_2 \times d_2}$, which takes an image of size $h_1 \times w_1$ and d_1 channels/slices (a CBCT image, in our particular case) and outputs another of size $h_2 \times w_2$ and d_2 channels/slices (a PlanCT image, in our case). A popular way to construct such a mapping is to use a DNN that learns (i.e., is trained) to construct mappings from a large set of data. The problem of synthesizing a PlanCT image that corresponds to a given CBCT image is highly ill-posed. That is, there is no unique “best” way to find the solution. Thus, we define what constitutes bad mappings in a quantitative way in terms of a loss function, whereby the DNN finds an approximate mapping that minimizes the loss function.

Due to computational limitations, we assume that the conversion mapping is uniform along the third dimension such that it can be approximated by a mapping $\mathbb{R}^{h_1 \times w_1} \rightarrow \mathbb{R}^{h_2 \times w_2}$. That is, our mapping converts CT images slice-by-slice along the z -axis.

Our strategy is largely based on CycleGAN [15], which simultaneously constructs four mappings:

- $G_{C \rightarrow P} : \mathbb{R}^{h_1 \times w_1} \rightarrow \mathbb{R}^{h_2 \times w_2}$, which takes a CBCT image and outputs a synthesized PlanCT image
- $G_{P \rightarrow C} : \mathbb{R}^{h_2 \times w_2} \rightarrow \mathbb{R}^{h_1 \times w_1}$, which takes a PlanCT image and outputs a synthesized CBCT image
- $D_P : \mathbb{R}^{h_2 \times w_2} \rightarrow \mathbb{R}^{h'_2 \times w'_2}$, which distinguishes synthesized PlanCT images from real ones
- $D_C : \mathbb{R}^{h_1 \times w_1} \rightarrow \mathbb{R}^{h'_1 \times w'_1}$, which distinguishes synthesized CBCT images from real ones.

The discriminator D_P looks at (overlapping) patches in a whole slice and determines whether each patch is likely to be one from a real image. Ideally, D_P would output the all-zero array $\mathbf{0}$ for synthesized PlanCT images and the all-one array $\mathbf{1}$ for real PlanCT images. The discriminator D_C works similarly for real and synthesized CBCT images.

We approximate these mappings by training a DNN for each mapping from a set **Plan** of PlanCT images and a set **CB** of CBCT images. The details of the dataset are given in §2.1. To this end, we formulate the desired properties of the mappings in terms of loss functions. Generators and discriminators have different sets of goals, and hence, different loss functions. Let $\|v\|_p$ denote the L_p -norm of a vector/array v . Our loss function for the discriminators based on [33] is as follows:

$$\begin{aligned} \text{Loss}_D = & \lambda_D \sum_{x \in \text{CB}} (\|D_P(G_{C \rightarrow P}(x)) - \mathbf{0}\|_2 + \|D_C(x) - \mathbf{1}\|_2) \\ & + \lambda_D \sum_{y \in \text{Plan}} (\|D_C(G_{P \rightarrow C}(y)) - \mathbf{0}\|_2 + \|D_P(y) - \mathbf{1}\|_2). \end{aligned}$$

The loss function forces D_P (and, respectively, D_C) to be trained to distinguish the distributions of real PlanCT (and, respectively, CBCT) images from synthesized ones.

Our loss function for generators $G_{C \rightarrow P}$ and $G_{P \rightarrow C}$ consists of several terms:

- $\text{Loss}_{\text{cycle}} = \text{Loss}_{\text{cycleA}} + \text{Loss}_{\text{cycleB}}$, where $\text{Loss}_{\text{cycleA}} = \sum_{x \in \text{CB}} \|x - G_{P \rightarrow C}(G_{C \rightarrow P}(x))\|_1$, $\text{Loss}_{\text{cycleB}} = \sum_{y \in \text{Plan}} \|y - G_{C \rightarrow P}(G_{P \rightarrow C}(y))\|_1$: This ensures that $G_{C \rightarrow P}$ and $G_{P \rightarrow C}$ are inverse mappings with respect to each other.
- $\text{Loss}_{\text{adv}} = \sum_{x \in \text{CB}} \|D_P(G_{C \rightarrow P}(x)) - \mathbf{1}\|_2 + \sum_{y \in \text{Plan}} \|D_C(G_{P \rightarrow C}(y)) - \mathbf{1}\|_2$: This encourages the generators to fool the discriminators by synthesizing realistic images.
- $\text{Loss}_{\text{grad}} = \sum_{x \in \text{CB}} (\|\partial_1(x - G_{C \rightarrow P}(x))\|_2 + \|\partial_2(x - G_{C \rightarrow P}(x))\|_2) + \sum_{y \in \text{Plan}} (\|\partial_1(y - G_{P \rightarrow C}(y))\|_2 + \|\partial_2(y - G_{P \rightarrow C}(y))\|_2)$, where (∂_1, ∂_2) is Sobel’s approximated gradient operator [13]. This encourages structural preservation before and after conversion by trying to keep the edges in the image.
- $\text{Loss}_{\text{idem}} = \sum_{x \in \text{CB}} \|G_{C \rightarrow P}(x) - G_{C \rightarrow P}(G_{C \rightarrow P}(x))\|_1 + \sum_{y \in \text{Plan}} \|G_{P \rightarrow C}(y) - G_{P \rightarrow C}(G_{P \rightarrow C}(y))\|_1$: This ensures that $G_{C \rightarrow P}^2 = G_{C \rightarrow P}$ and $G_{P \rightarrow C}^2 = G_{P \rightarrow C}$ (i.e., that they are idempotent).

The terms $\text{Loss}_{\text{cycle}}$ and $\text{Loss}_{\text{idem}}$ pertain to mathematical requirements regarding what the conversion mappings should satisfy, and they help to increase the stability during training. The terms $\text{Loss}_{\text{grad}}$ and Loss_{adv} are competing demands as the former stipulates that the generator preserves the structure of the input image while the latter encourages altering the input image to look more like a real one. In the end, they should find a good balance.

We combine these terms by taking the weighted sum with respect to the hyper-parameters λ :

$$\text{Loss}_G = \lambda_{\text{cycle}} \text{Loss}_{\text{cycle}} + \lambda_{\text{adv}} \text{Loss}_{\text{adv}} + \lambda_{\text{grad}} \text{Loss}_{\text{grad}} + \lambda_{\text{idem}} \text{Loss}_{\text{idem}}$$

and use stochastic gradient descent to find a (local) minimizer of the combined loss function. In practice, we can add more terms as regularizers to exploit prior knowledge from the image domains, such as the total variation and air–body boundary preservation. See our implementation [1] for details.

2.2.1. Technical details The intensity of CT images was clipped to $[-500, 200]$ HU, and scaled to $[-1, 1]$. That is, the pixels with an HU of less than -500 were all mapped to -1, and those with an HU of higher than 200 were all mapped to 1. When fed into the network, the images were cropped randomly around the center to a size of 480×384 . This size was selected such that the body was always contained well inside the edges in order to avoid the boundary effects of convolutional neural networks in general.

For the generators G_* , we used an encoder–decoder network as follows:

- (i) One convolution layer with a 7×7 kernel with stride 1,
- (ii) followed by three down convolution layers with a 3×3 kernel with stride 2 and channels 32, 64 and 128,
- (iii) followed by 9 residual blocks with a 3×3 kernel with stride 1,
- (iv) followed by three up-sampling layers each consisting of an unpooling with stride 2 followed by a residual block with a 3×3 kernel with stride 1,
- (v) followed by a convolution layer with a 7×7 kernel with stride 1.

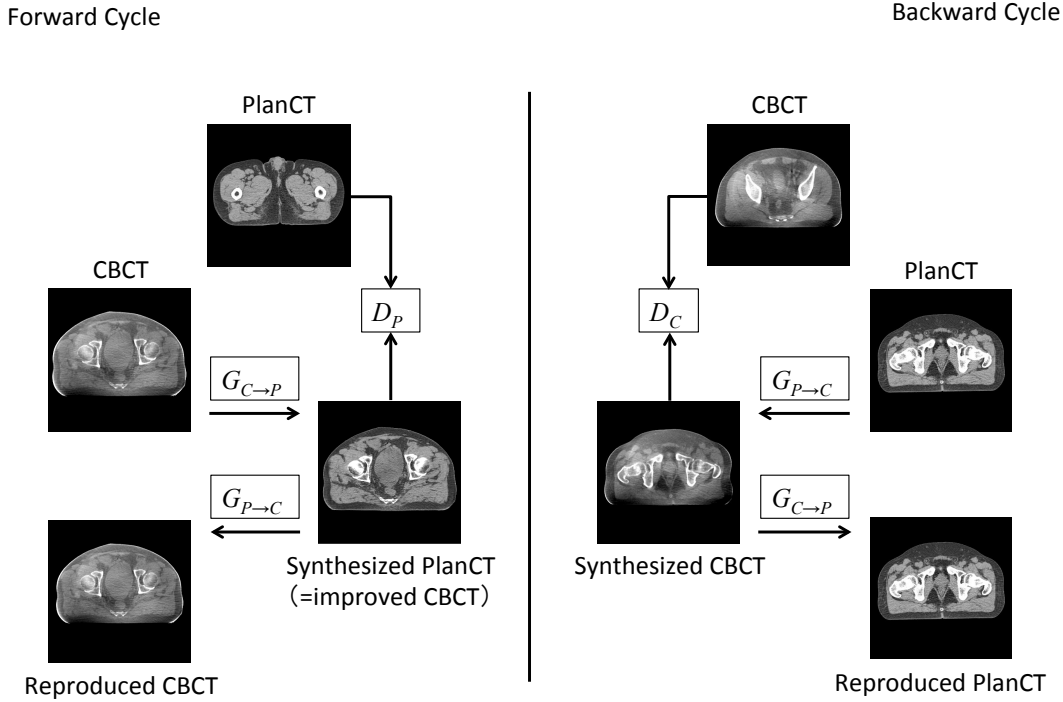


Figure 1. Overview of the CycleGAN model with a forward cycle and a backward cycles.

Except for the last layer, we used the rectified linear unit for activation, and instance normalization [7] for normalization. The last layer was equipped with the hyperbolic tangent as activation and without normalization. Layers (i),(ii) and (iv),(v) have skip connections [22] to transfer the structure of the input image directly.

For the discriminators D_* , we used a typical down convolution network as follows:

- (i) Three down convolution layers with a 4×4 kernel with stride 2 and channels 32, 64 and 128,
- (ii) followed by a convolution layer with a 4×4 kernel with stride 1 and channel 256,
- (iii) followed by a convolution layer with a 4×4 kernel with stride 1 and channel 1.

We used a leaky rectified linear unit with slope 0.2 for activation, and instance normalization for normalization in all but the last layer. We did not apply any activation and normalization to the last layer. The receptive field of the network was 70×70 and each pixel in the output revealed the evaluation for the patch of this size in the input image. We also experimented with different network configurations by modifying the kernel size of each layer and the total number of layers, and thus with different receptive field sizes, and observed that the above configuration performs well.

In both the generators and the discriminators, it is important to use instance normalization without an affine transform; with an affine transform, we observed that the output images tended to have low voxel values in certain regions. The padding value for the first layer was

selected to match the intensity of the air (-1 , in our case).

We chose the hyper-parameters empirically as follows: $\lambda_{cycle} = 10.0$, $\lambda_{adv} = 1.0$, $\lambda_{grad} = 0.1$, $\lambda_{idem} = 1.0$, $\lambda_D = 1.0$. All networks were trained from scratch at a learning rate of 10^{-4} , with the Adam optimizer with a batch size of 1. We kept the same learning rate for the first 25 epochs, and linearly decayed the rate to zero over the next 25 epochs.

Note that for generators, minimizing $Loss_{adv}$ means maximizing $Loss_D$, and for discriminators, minimizing $Loss_D$ means maximizing $Loss_{adv}$. Generators and discriminators are adversarial, trying to beat each other. If the competition is nearly even, they both improve in a steady manner. Therefore, when training GANs, their strength must be balanced. There are several ways to help to maintain this balance:

- tuning the weightings λ_{adv} and λ_D ,
- using different loss functions (e.g., Wasserstein GAN with a gradient penalty [12]),
- scheduling updates for the generator and discriminator (e.g., updating the generator only once for every five updates of the discriminator),
- tuning the degrees of freedom of the networks for the generators and discriminators,
- and defining good stopping criteria.

Although it was unfeasible to try all the possibilities, we observed that the last one had the most significant effect. We thus adjusted the number of channels in each network. Although Wasserstein GANs are believed to be very helpful, in our experiments we could not find a good configuration for our particular problem. Therefore, we decided to stick to the current loss function. Similarly, it was appropriate to set $\lambda_{adv} = \lambda_D$ and to update the generators and discriminators in equal frequency. The point at which learning stopped was also important. We noticed that if we trained too many epochs, the preservation of anatomical structures began to deteriorate. We watched the learning progress by visually inspecting the output, and decided to train 50 epochs for this study. However, this number should be dependent on the dataset. Establishing judicious stopping criteria remains for future research.

The weights of the neural networks were randomly initialized using Hes method [16]. In order to mitigate instability in the initialization, we set the first 200 iterations as a warmup period. During the warmup, we set $\lambda_{adv} = 0$, and added an extra term $Loss_{id} = \sum_{x \in \mathbf{CB}} \|x - G_{C \rightarrow P}(x)\|_2 + \sum_{y \in \mathbf{Plan}} \|y - G_{P \rightarrow C}(y)\|_2$ to $Loss_G$. This means that the generators first learn the identity mapping, and then proceed to learn the desired conversion. The loss function for the discriminator remains unmodified during the warmup period. Note that during the initial stage, discriminators output nonsense, so it does not make sense to use $Loss_{adv}$ to train the generators.

2.3. Environment and timing

We conducted experiments with a personal computer equipped with a single GPU (Nvidia 1080Ti) and a CPU (Intel Core i7-6950X) with 132 GB memory, running Ubuntu 18.04.1 LTS. We implemented our algorithm with Python 3.6.6 and Chainer 5.0.0 [28]. Our codes are

available on Github [1]§

The training required approximately 20 minutes per epoch (2795 iterations), and 13 hours for 50 epochs. The conversion required about 6 s for one volume of data (32 slices per second).

2.4. Evaluation method

CBCT and PlanCT image pairs from 4 out of 20 prostate cancer patients were used for the quantitative evaluation. The resulting SynPlanCT images were compared to the original CBCT and PlanCT images using the Hounsfield Unit (HU) statistic and visual inspection of the regions of interest (ROIs) from four different types of tissues (viz., prostate, bladder, muscle, and fat). For a quantitative evaluation of the muscle and fat regions, four slices were selected, one slice from each of the four patients. Four square ROIs with 10×10 pixels were arbitrary positioned in the regions of the same soft tissue area (fat or muscle) in distant locations on a selected slice (Figure 2). Four slices at 3 mm intervals per patient were selected for the prostate region. Four slices at 6 mm intervals per patient were selected for the bladder region. One square ROI with 10×10 pixels was arbitrary positioned in the regions of the same soft tissue area (prostate or bladder) on a selected slice. These ROIs were positioned on the corresponding slices and locations of CBCT and PlanCT images. That is, 16 ROIs were positioned for each soft tissue to evaluate the distribution of the average HU of each ROI. To determine the robustness of our method, for each evaluation slice we produced five SynPlanCT images from five network models trained with the same structure and hyper-parameters. That is, the SynPlanCT images were evaluated with a total of 80 ROIs.

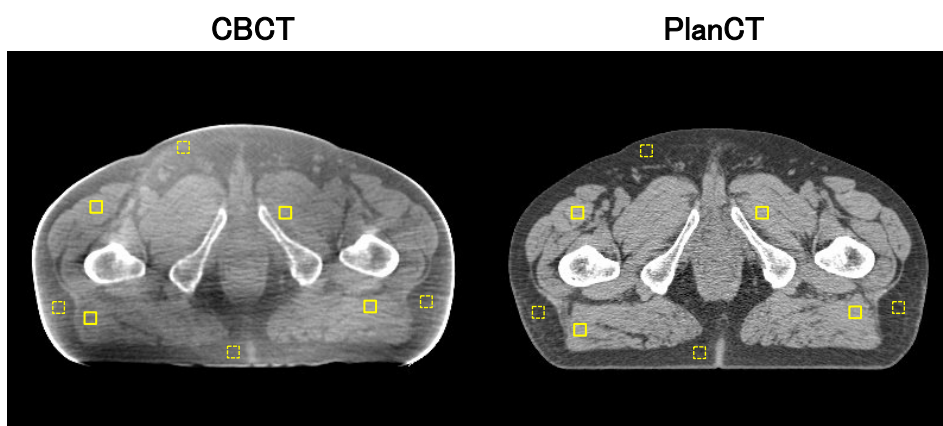


Figure 2. Example of evaluating the ROI distribution: (left) four muscle ROIs (solid square) and four fat ROIs (dotted square) placed on a selected slice of CBCT for test patient (i); and (right) corresponding ROIs placed on a corresponding slice of PlanCT of the same patient.

§ For the CycleGAN code, we based our implementation on <https://github.com/~naoto0804/~chainer-cyclegan>.

3. Results

3.1. Comparison of Image qualities and Preservation of anatomical structures

The axial, sagittal, and coronal slices of CBCT, SynPlanCT and PlanCT for two representative cases (test patients (i) and (ii)) are shown in Figure 3. The image quality of SynPlanCTs for all three planes show substantial improvement in terms of voxel values, spatial uniformity, artifact suppression, compared to those of original CBCT. The histograms of SynPlanCT images are also much closer to those of the PlanCT images, with better differentiation between fat and muscle, compared to those of CBCT images, as shown in Figure 4.

As shown in Figure 5, edge sharpness and structure were preserved in not only large bulky tissues, such as the rectum and bladder, but also in small isolated structures, such as the small intestine and intestinal gas. High-frequency artifacts such as streaks and rings could not be completely removed, but they were considerably suppressed. In this study, despite learning with only axial slices, owing to computational limitations, there was no outstanding problem in the continuity of the structure and voxel values in the other two planes (coronal and sagittal), as shown in Figure 3.

3.2. Quantitative evaluation

The mean and the difference of the maximum and minimum average HU of each ROI positioned in the four evaluation tissues in PlanCT, SynPlanCT, and CBCT are summarized in Table 1, where the average HU of an ROI refers to the average voxel value of 10×10 pixels in the ROI. The difference in the average HU for the four evaluation tissues between SynPlanCT and PlanCT (muscle: 6HU, fat: 0HU, prostate: 3HU, bladder: 2HU) were substantially suppressed compared to those between the original CBCT and PlanCT (muscle: 230HU, fat: 161HU, prostate: 201HU, bladder: 180HU). Figure 6 shows a comparison of the original CBCT, SynPlanCT, and PlanCT in the distribution of the average HU of each muscle ROI as an example. The variance of the average HU of each muscle ROI for SynPlanCT is much closer to that for PlanCT compared to that for CBCT. Figure 7 shows comparisons between the SynPlanCT and the PlanCT in the distribution of the average HU of each ROI positioned in the four evaluation tissues. The variance of the average HU of each ROI positioned in the four evaluation tissues for SynPlanCT was larger than those for PlanCT. There were a few ROIs with specifically high HU in fat and low HU in the prostate. Figure 8 compares the distributions of the average HU of each ROI positioned in the four evaluation tissues of each of the five SynPlanCT images, synthesized using the five network models trained with the same structure and hyper-parameters (m1–m5) and those of PlanCT. Note that SynPlanCT images used in Figure 3–7 and Table 1 were synthesized by applying network model (m1). The average HU differed by 10 HU or less for all of the four evaluation tissues in the five SynPlanCT images. However, there were a few ROIs with specifically high HU in fat and specifically low HU in the prostate for the SynPlanCT images from some network models, as shown in Figure 8. Figure 9 compares CBCT and SynPlanCT images synthesized by applying network model (m1) to test patient (i), as an example. We found that the voxel values of the

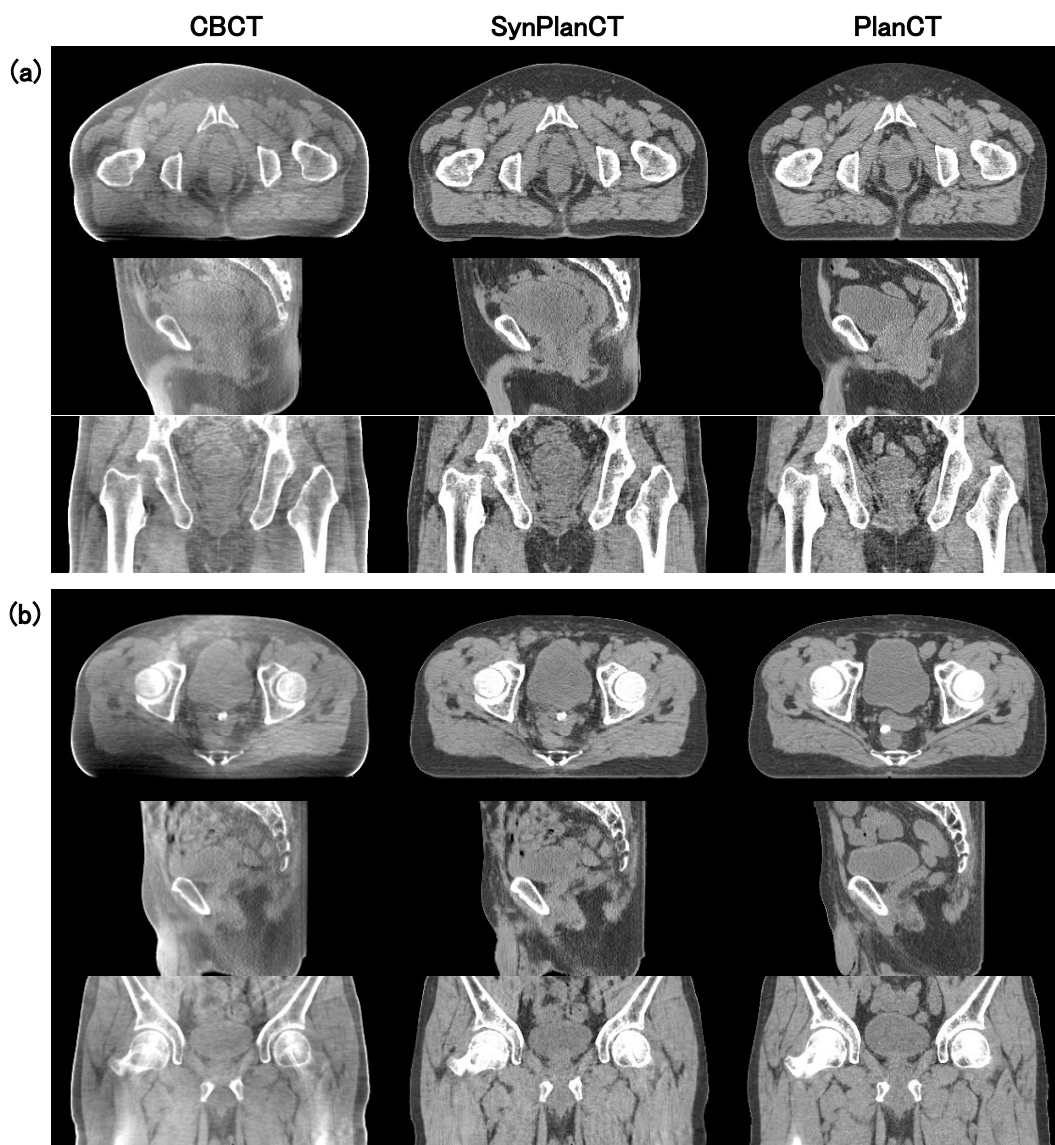


Figure 3. Comparison of the image quality among CBCT, SynPlanCT, and PlanCT: (a) test patient (i) and (b) test patient (ii). For each patient, the images in the top, middle, and bottom row are axial, coronal, and sagittal views, respectively. The images on the left, middle, and right are CBCT, SynPlanCT and PlanCT, respectively. The display window range was set to (-400, 0) HU for CBCT and (-200, 200) HU for SynPlanCT and PlanCT.

SynPlanCT images were higher in the region around the fat ROI shown in Figure 9(b), and lower in the region around the prostate ROI shown in Figure 9(d). High signal artifacts were observed, originally in the fat region of the CBCT image (Figure 9(a)), and it seemed that the artifacts were not sufficiently suppressed on SynPlanCT images from some network models (e.g., m1–m3). On the other hand, low signal artifacts were observed originally in the prostate region of the CBCT image (Figure 9(c)), but it is difficult to determine whether this low signal is an artifact or a tissue feature. It may be important in terms of structural preservation to preserve subtle contrasts, when it is difficult to demarcate artifacts from tissue.

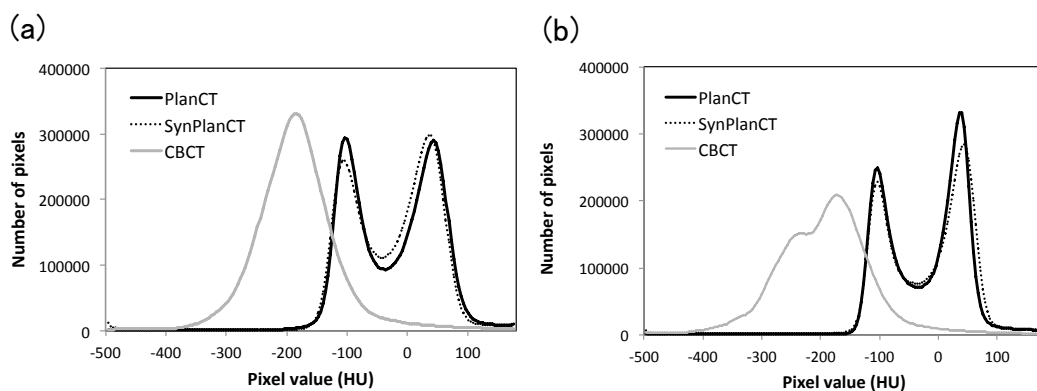


Figure 4. Image histograms for PlanCT (black line), SynPlanCT (solid black line), and CBCT (grey line) for test patients (i) and (ii).

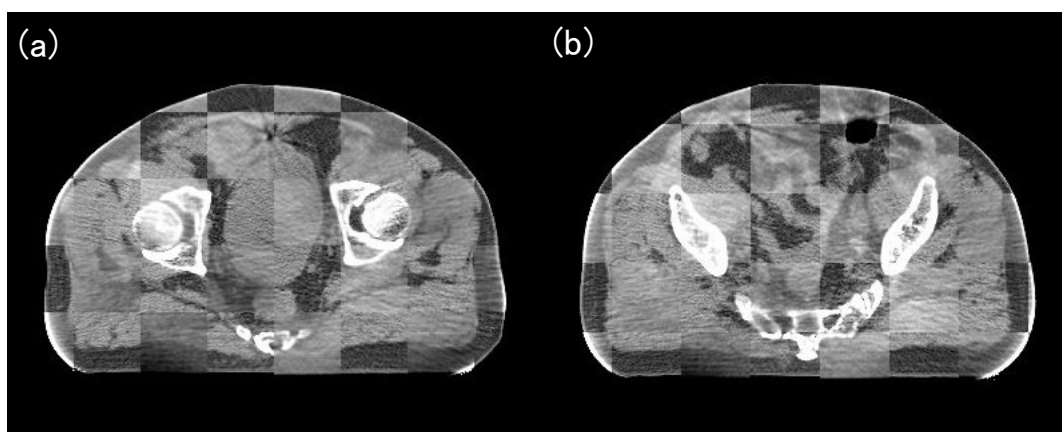


Figure 5. Checkerboard images of a CBCT image and SynPlanCT image: (a) bladder and rectum slice, and (b) small intestine slice.

| | | PlanCT (HU) | SynPlanCT (HU) | CBCT (HU) |
|----------|---------|-------------|----------------|-----------|
| Muscle | mean | 50 | 44 | -180 |
| | max-min | 23 | 44 | 268 |
| Fat | mean | -103 | -103 | -264 |
| | max-min | 27 | 83 | 218 |
| Prostate | mean | 34 | 31 | -167 |
| | max-min | 22 | 45 | 42 |
| Bladder | mean | 13 | 11 | -167 |
| | max-min | 22 | 34 | 41 |

Table 1. Mean and difference in maximum and minimum average HU of each ROI positioned in the four evaluation tissues in PlanCT, SynPlanCT, and CBCT.

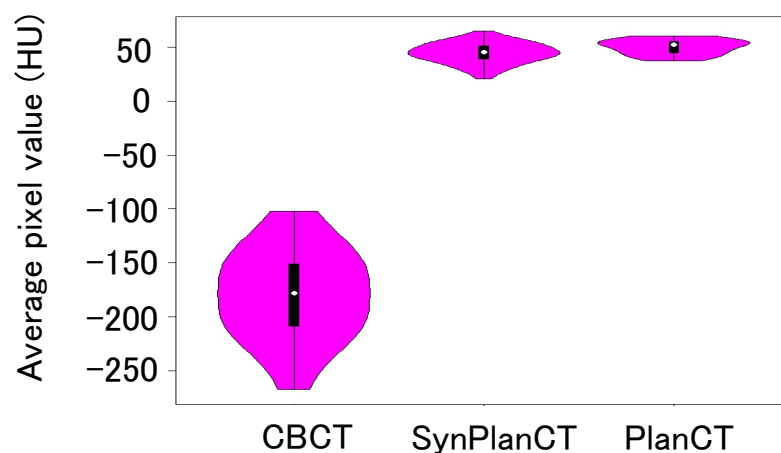


Figure 6. Comparison of the distribution of average HU in muscle ROIs among CBCT, SynPlanCT, and PlanCT.

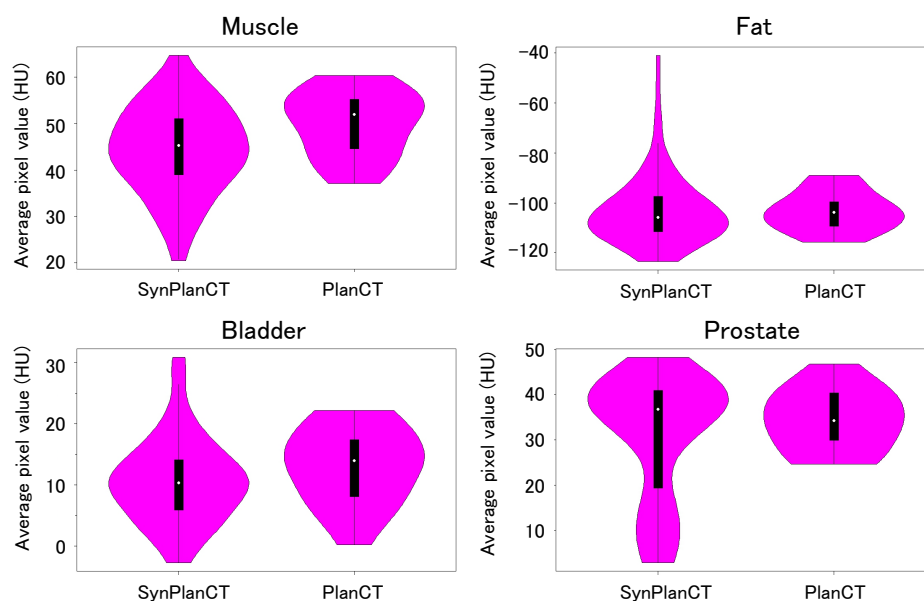


Figure 7. Comparison of the distribution of the average HU of each ROI positioned in the four evaluation tissues (upper-left, muscle; upper-right, fat; lower-left, bladder; lower-right, prostate) between SynPlanCT and PlanCT.

4. Discussion

We developed a CycleGAN-based method to synthesize PlanCT-like images from CBCT images. In contrast to previous work using PlanCT on the same patient as prior information, the proposed method does not in principle require accurate spatially aligned CBCT and PlanCT volume pairs from the same patients. In this study, models were trained with CBCT and PlanCT images of the same patients, and these images were rigidly registered to include

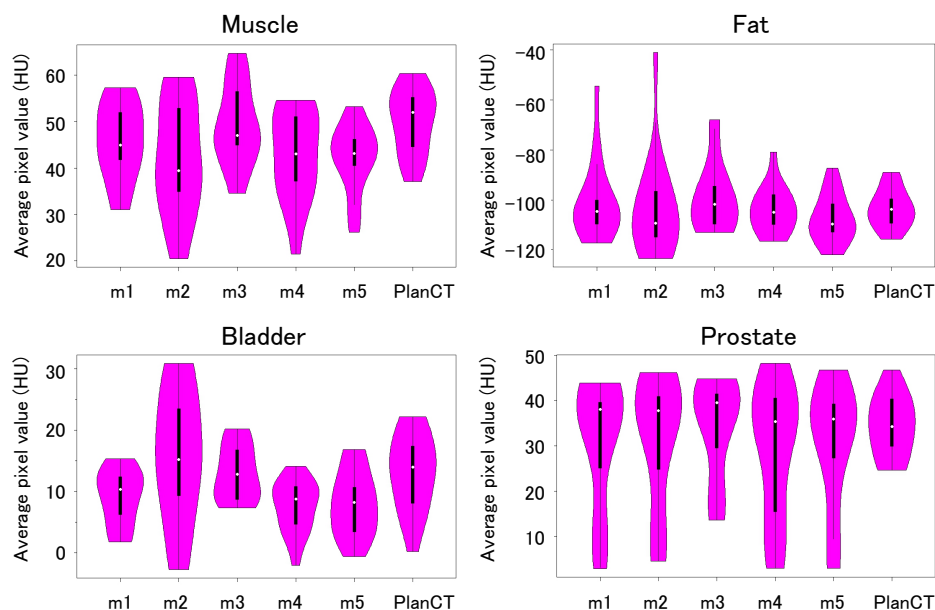


Figure 8. Comparison of the distribution of the average HU of each ROI positioned in the four evaluation tissues for each of the five SynPlanCT images from five network models trained with the same structure and hyper-parameters (m1–m5) and those of PlanCT for comparison.

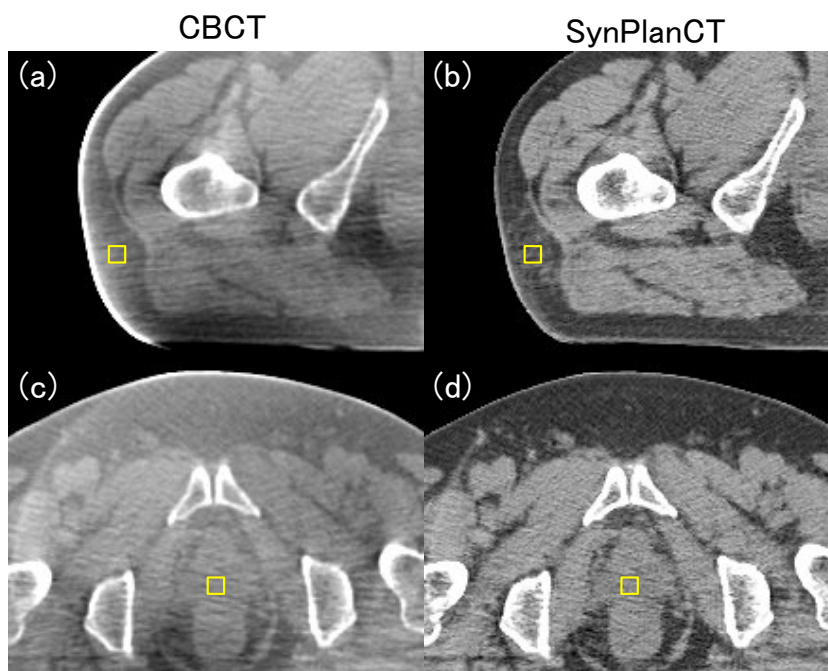


Figure 9. Example of ROIs in which the average HU is particularly high or low: (top) fat ROIs on a selected CBCT slice and a corresponding SynPlanCT slice; and (bottom) prostate ROIs on selected CBCT and a corresponding SynPlanCT slice.

bodies of all patients in a cropped calculation area around the center, in the size of 480×384 (pixels) for efficient calculation. During the training process of CycleGAN, the discriminators were provided randomly selected unpaired and unaligned images, rather than aligned paired

images. Therefore, registration between CBCT and PlanCT should not affect the image quality of synthesized PlanCT. In addition, by virtue of PatchGAN, the discriminators look only at a small patch and try to determine whether each patch in an image is real or fake, canceling the effects of rigid registration. In fact, when using non-aligned CBCT and PlanCT volume pairs from the same patient, which were shifted randomly to each other by 50 pixels or more, the image quality improved and the structure was better preserved with similar quality to those of the aligned ones. This result shows that the proposed method does not require aligned volume datasets. Furthermore, in order to evaluate learning with completely unpaired and unaligned images, 16 patients for training were divided into two groups. Then, the network model was trained with CBCT images of eight patients and PlanCT images of the other eight patients. This model showed similar improvement in voxel values, spatial uniformity, and artifact suppression on SynPlanCT images, but the structures were incorrectly synthesized in some slices. The failure to preserve the structures may be caused by over-learning due to the reduction by half of the learning data. We assume that simply increasing the amount of learning data would resolve the issue.

In evaluating a medical application for a DNN, the following three points of view are important.

- Accuracy: the output of the method is close to the ground truth, which is often clinically unavailable.
- Precision: the method is robust and produces stable outputs. In general, DNN-based methods inevitably involve randomness when initializing the weights of the networks and during the learning process. Hence, even with the same parameters and the same dataset, their outcome can never be same.
- Generalization: the method works with different datasets acquired in different ways.

To evaluate the accuracy of our method ideally, we would compare SynPlanCT images with PlanCT images acquired completely simultaneously with CBCT images, though these are obviously unavailable. Hence, we focused on two types of accuracy to the output SynPlanCT in this study: preservation of anatomical structures compared with CBCT, and image quality compared with PlanCT.

Preserving anatomical structures is crucial for image-improvement methods using unpaired and unaligned CBCT and PlanCT datasets. In previous work using PlanCT as prior information, high-frequency artifacts such as streaks, blurred edges, deformations, and missing anatomical structures were left as problems to be solved [17, 11, 2, 25]. In this study, the image quality of CBCT improved while suppressing high-frequency artifacts and preserving the anatomical structures of CBCT. Designing the size of the receptive field of the PatchGAN discriminator is important for preserving the structure and concurrently converting the voxel values. When the receptive field is set too large, learning with a DNN is influenced by the structure and placement of the organs of individual patients. That is, it is overlearning. On the other hand, when the receptive field is too small, the local structural pattern cannot be detected, and only the voxel values are converted, ignoring the structure. The 70×70 receptive fields of the discriminator used in this study can detect typical local

structural patterns commonly found in all patients, enabling the conversion of voxel values while preserving the structure.

Moreover, despite learning with only axial slices, due to computational limitations, there was no outstanding problem in the continuity of the structure and voxel values in the other two planes (coronal and sagittal). Such continuity along the other two planes is evidence that the anatomical structure was correctly preserved within the axial images. In future work, we will investigate how learning directly with volume data can affect the continuity of voxel values and the preservation of anatomical structures.

The image quality of SynPlanCT showed substantial improvement in terms of voxel values, spatial uniformity, and artifact suppression compared to those of the original CBCT. As shown in Table 1, the differences in the maximum and minimum average HUs of muscle and fat ROIs on SynPlanCT (44 and 83 HU) were much smaller than those of the original CBCT (268 and 218 HU), while those of prostate and bladder ROIs on SynPlanCT (45 and 34 HU) and CBCT (42 and 41 HU) were relatively close. This result means that various artifacts, such as rings, streaks, and shading have a stronger effect on muscle and fat, spreading throughout the entire CBCT image, than in the prostate and bladder, located near the center of the image, and indeed the artifacts were effectively suppressed by the proposed method. In this study, voxel values of CBCT and PlanCT images were clipped to $[-500, 200]$ for efficient calculation. Thus, the voxel values of bone, which are more than 200 HU, were not evaluated quantitatively. In future work, we will expand the range of voxel values used for learning and quantitatively evaluate the improvement in voxel values of bone.

In order to assess the precision of our method, we compared five models trained with the same structure and hyper-parameters, but trained with different random initial weights and stochastic gradient descent. We observed acceptable fluctuation of less than 10 HU (Figure 8). Note that we did observe on one occasion that models trained with the same hyper-parameters produced totally different images. Although it is customary in medical applications of DNNs to present results from only the best models, we here provide an extreme example in which the generators completely failed to learn a meaningful mapping and produced totally distorted images (see Figure 10). In our method, this type of failure was mitigated by introducing a warmup period during the learning process, as discussed in §2.2.1, which helped to increase the overall robustness. Even after proper training, it is impossible to ensure that the DNN will always produce feasible outputs. Thus, it is more important to detect and alert the user when a failure may have occurred. We can use the cycle consistency $\text{Loss}_{\text{cycleA}}$ (see §2.2) as a measure of the soundness of our networks’ output. Such failures in training (e.g., see Figure 10) can be detected as a high value of $\text{Loss}_{\text{cycleA}}$, namely, when this is more than three times that when training was successful. Recall that $\text{Loss}_{\text{cycleA}}$ is a summary of the difference in the voxel values of the CBCT image x and the cyclically translated image $G_{P \rightarrow C}(G_{C \rightarrow P}(x))$. We can look directly at a so-called difference image $G_{P \rightarrow C}(G_{C \rightarrow P}(x)) - x$ to locate where the violation of cycle consistency occurred. In fact, we noticed that it is more suitable to look at the difference in the gradient rather than in the voxel values. As such, we define the *cycle*

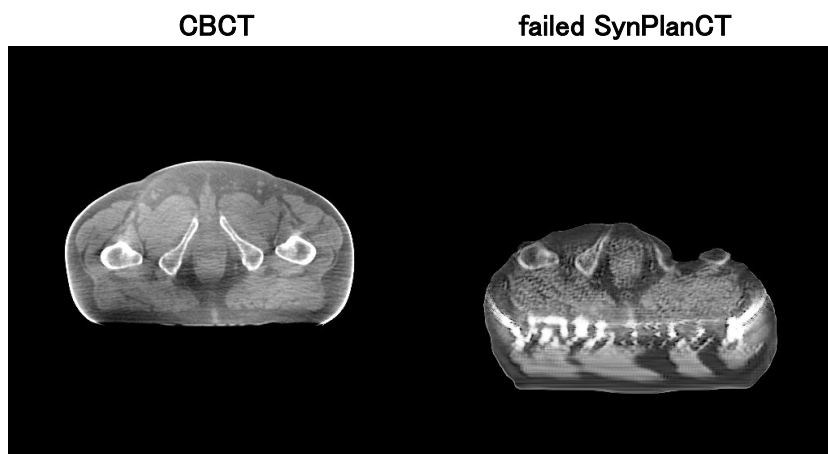


Figure 10. Example of a failed SynPlanCT image from some network model: (left) original CBCT image, and (right) failed SynPlanCT image.

difference image as

$$\|(\partial_1(G_{P \rightarrow C}(G_{C \rightarrow P}(x))), \partial_2(G_{P \rightarrow C}(G_{C \rightarrow P}(x))))\|_2 - \|(\partial_1(x), \partial_2(x))\|_2,$$

where ∂_1, ∂_2 are Sobel's gradient operators, discussed in §2.2. If both generators $G_{C \rightarrow P}$ and $G_{P \rightarrow C}$ work perfectly, the cycle difference image should constantly be zero. Thus, we can use this cycle difference image to check how and where the generators may have failed. To demonstrate this, we selected a pair of successfully learned models $G_{C \rightarrow P}$ and $G_{P \rightarrow C}$ and an input image x containing metal seeds and a couch, which were not seen in the training data. The cycle difference image clearly indicates anomalous objects that were not learned during training (Figure 11). This result shows that we can use the cycle difference as a simple safeguard against failures both in training and inference.



Figure 11. Example of cycle difference: (left) original CBCT image containing metal seeds, (middle) cyclically translated image, and (right) their difference in the gradient.

There are two possible directions in which our method can be generalized. We believe that the proposed method works properly with CBCT and PlanCT image datasets acquired in other institutions. In addition, the proposed method should improve the image quality of organs other than the pelvis. These two directions will be pursued in future research.

5. Conclusion

We developed a synthetic approach based on CycleGAN to produce SynPlanCT images from CBCT images. The proposed approach relies only on unpaired and unaligned CBCT and PlanCT images for training. The image quality of the synthesized PlanCT images substantially improved in terms of voxel values, spatial uniformity, and artifact suppression compared to those of the original CBCT. The anatomical structures of the original CBCT were well preserved in SynPlanCT. In order to demonstrate the robustness of our method, we compared five models trained with the same structure and hyper-parameters, and observed an acceptable fluctuation of less than 10 HU. The proposed method may be applied directly to 3D CBCT images reconstructed from a commercial CBCT scanner with high computational efficiency. The proposed method may enable soft tissue details to be more easily visualized and the use of CBCT images for patient-specific treatment and dose calculation in radiotherapy.

Acknowledgments

Kaji was partially supported by JST PRESTO, Grant Number JPMJPR16E3 Japan. Nawa was partially supported by a JSPS Grant-in-Aid for Young Scientists (B), 17K15799. Imae was partially supported by a JSPS Grant-in-Aid for Scientific Research (C), 18K07667. Nakamoto was partially supported by a JSPS Grant-in-Aid for JSPS Fellows, 18J00599, and a Grant-in-Aid for Early-Career Scientists, 18K15625. Ohta was partially supported by a JSPS Grant-in-Aid for Early-Career Scientists, 18K15583.

This study was partially funded by Canon Medical Systems Corporation.

References

- [1] *Image translation by CNNs trained on unpaired data*, <https://github.com/shizuo-kaji/UnpairedImageTranslation>, 2019.
- [2] Oyama A, Kumagai S, Arai N, Takata T, Saikawa Y, Shiraishi K, Kobayashi T, and Kotoku J, *Image quality improvement in cone-beam ct using the super-resolution technique*, *J. Radiat. Res.* **59** (2018), 501.
- [3] Sisniega A, Zbijewski W, Badal A, Kyprianou IS, Stayman JW, Vaquero JJ, and Siewerdsen JH, *Monte carlo study of the effects of system geometry and antiscatter grids on cone-beam CT scatter distribution*, *Med. Phys.* **40** (2013), 051915.
- [4] Letourneau D, Martinez AA, Lockman D, Yan D, Vargas C, Ivaldi G, and Wong J, *Assessment of residual error for online cone-beam CT-guided treatment of prostate cancer patients*, *Int. J. Radiat. Oncol. Biol. Phys.* **62** (2005), 1239.
- [5] Nie D, Trullo R, Lian J, Petitjean C, Ruan S, Wang Q, and Shen D, *Medical image synthesis with context-aware generative adversarial networks*, *Medical Image Computing and Computer Assisted Intervention (MICCAI)*, vol. 10435, 2017, p. 417.
- [6] Paquin D, Levy D, and Xing L, *Multiscale registration of planning CT and daily cone beam CT images for adaptive radiation therapy*, *Med. Phys.* **36** (2009), 4.
- [7] Ulyanov D, Vedaldi A, and Lempitsky V, *Instance normalization: The missing ingredient for fast stylization*, arXiv:1607.08022, 2017.
- [8] Jaffray DA, Siewerdsen JH, Wong JW, and Martinez AA, *Flat-panel cone-beam computed-tomography for image-guided radiation therapy*, *Int. J. Radiat. Oncol. Biol. Phys.* **53** (2002), 1337.

- [9] Fove X et al, *Can radiomics features be reproducibly measured from CBCT images for patients with non-small cell lung cancer?*, Med. Phys. **42** (2015), 6784.
- [10] Kurz C et al, *Investigating deformable image registration and scatter correction for CBCT-based dose calculation in adaptive impt*, Med. Phys. **43** (2016), 5635.
- [11] Kidar HS and Azizi H, *Assessing the impact of choosing different deformable registration algorithms on cone-beam ct enhancement by histogram matching*, Radiat. Oncol. **13** (2018), 217.
- [12] Gulrajani I, Ahmed F, Arjovsky M, Dumoulin V, and Courville A, *Improved training of wasserstein gans*, Advances in Neural Information Processing Systems (NIPS), 2017.
- [13] Sobel I and Feldman G, *An isotropic 3x3 image gradient operator*, Stanford Artificial Intelligence Project (SAIL), 1968.
- [14] Wolterink JM, Dinkla AM, Savenije MH, Seevinck PR, van den Berg CA, and Isgum I, *Deep mr to ct synthesis using unpaired data*, International Workshop on simulation and Synthesis in Medical Imaging (SASHIMI), 2017, p. 14.
- [15] Zhu JY, Park T, Isola P, and Efros AA, *Unpaired image-to-image translation using cycle-consistent adversarial networks*, The IEEE International Conference on computer vision (ICCV), 2017.
- [16] He Kaiming, Zhang Xiangyu, Ren Shaoqing, and Sun Jian, *Delving deep into rectifiers: Surpassing human-level performance on imagenet classification*, Proceedings of the 2015 IEEE International Conference on Computer Vision (ICCV) (Washington, DC, USA), ICCV '15, IEEE Computer Society, 2015, pp. 1026–1034.
- [17] Shi L, Tsui T, Wei J, and Zhu L, *Fast shading correction for cone beam ct in radiation therapy via sparse sampling on planning ct*, Med. Phys. **44** (2017), 1796.
- [18] Gukenberger M, Meyer J, Vordermark D, Baier K, Wilbert J, and Flentje M, *Magnitude and clinical relevance of translational and rotational patient setup errors: a cone-beam CT study*, Int. J. Radiat. Oncol. Biol. Phys. **65** (2006), 934.
- [19] Stock M, Pasler M, Birkfellner W, Homolka P, Poetter R, and Georg D, *Image quality and stability of image-guided radiotherapy (IGRT) devices: a comparative study*, Radiother. Oncol. **93** (2009), 1.
- [20] Sun M and Star-Lack JM, *Improved scatter correction using adaptive scatter kernel superposition*, Phys. Med. Biol. **55** (2010), 6695.
- [21] Mazurowski MA, Buda M, Saha A, and Bashir MR, *Deep learning in radiology: an overview of the concepts and a survey of the state of the art*, arXiv:1802.08717, 2018.
- [22] Ronneberger O, Fischer P, and Brox T, *U-net: Convolutional networks for biomedical image segmentation*, Medical Image Computing and Computer-Assisted Intervention - MICCAI. Lecture Notes in Computer Science. Navab N, Hornegger J, Wells W and Frangi A (ed), vol. 9351, Springer, 2015, p. 234.
- [23] Isola P, Zhu JY, Zhou T, and Efros AA, *Image-to-image translation with conditional adversarial networks*, IEEE/CVF Conference on Computer Vision and Pattern Recognition (CVPR), 2017.
- [24] Zhang R, Isola P, and Efros AA, *Colorful image colorization*, European conference computer vision (ECCV), 2016.
- [25] Kida S, Nakamoto T, Nakano M, Nawa K, Haga A, Kotoku J, Yamashita H, and Nakagawa K, *Cone beam computed tomography image improvement using a deep convolutional neural network*, Cureus **10** (2018).
- [26] Kim S, Yoo S, Yin FF, Samei E, and Yoshizumi T, *Kilovoltage cone-beam CT: comparative dose and image quality evaluation in partial and full-angle scan protocols*, Med. Phys. **37** (2010), 3648.
- [27] Klein S, Staring M, Murphy K, Viergever MA, and Pluim JPW, *Elastix: a toolbox for intensity-based medical image registration*, IEEE. Trans. Med. Imaging. **29** (2010), 196.
- [28] Tokui S, Oono K, Hido S, and Clayton J, *Chainer: a next-generation open source framework for deep learning*, Proceedings of Workshop on Machine Learning Systems (LearningSys) in The Twenty-ninth Annual Conference on Neural Information Processing Systems (NIPS), 2015.
- [29] Park SB, Rhee FC, Monroe JI, and Sohn JW, *Spatially weighted mutual information image registration for image guided radiation therapy*, Med. Phys. **37** (2010), 4590.
- [30] Higaki T, Nakamura Y, Tatsugami F, Nakaura T, and Awai K, *Improvement of image quality at ct and mri using deep learning*, Jpn. J. Radiol. **29** (2018), 1.
- [31] Stankovic U, Ploeger LS, van Herk M, and Sonke JJ, *Optimal combination of anti-scatter grids and*

- software correction for CBCT imaging*, Med. Phys. **44** (2017), 4437.
- [32] van Timmeren JE, Leijenaar RTH, van Elmpt W, Reymen B, and Lambin P, *Feature selection methodology for longitudinal cone-beam CT radiomics*, Acta. Oncol. **56** (2017), 1537.
- [33] Mao X, Li Q, Xie H, Lau RYK, Wang Z, and Smolley SP, *On the effectiveness of least squares generative adversarial networks*, arXiv:1712.06391, 2018.
- [34] Wang X, Li J, Wang P, Yuan K, Yin G, and Wan B, *Image guided radiation therapy boost in combination with high-dose-rate intracavitary brachytherapy for the treatment of cervical cancer*, Brachytherapy **8** (2016), 122.
- [35] Zhang Z, Yang L, and Zheng Y, *Translating and segmenting multimodal medical volumes with cycle- and shape-consistency generative adversarial network*, arXiv:1802.09655, 2018.